Journal of Hydroscience and Hydraulic Engineering
Vol. 16, No. 2, November, 1998, 71-81

DEVELOPMENT OF HIGH-RESOLUTION 3D PTV TECHNIQUE WITH LASER-LIGHT SHEET SCANNINGS

By

Satoru Ushijima

Central Research Institute of Electric Power Industry (CRIEPI)

1646 Abiko, Abiko-shi, Chiba-ken, 270-11, JAPAN
ushijima@criepi.denken.or.jp

SYNOPSIS

This paper describes the development of the three-dimensional particle tracking velocimetry (3D PTV) technique which enables us to obtain remarkably larger number of velocity vectors than previous techniques. In contrast to the usual stereoscopic image recordings, the present 3D PTV visualizes an entire three-dimensional flow using the scanning laser-light sheets generated from a pair of optical scanners and the images are taken by a high-speed video system synchronized with the scannings. The digital image analyses to derive velocity components are based on the numerical procedure as done by Ushijima and Tanaka (1), in which several improvements have been made on the extraction of particle images, the determination of their positions, the derivation of velocity components and others. The present 3D PTV was applied to the rotating fluids accompanied by Ekman boundary layers and their complicated secondary flow patterns as well as the primary circulations are quantitatively captured. In addition, the measured flow patterns agree well with three-dimensional computational results.

INTRODUCTION

Digital image processing has been extensively utilized to analyze flow-visualization images to understand large scale structures and various spatial characteristics. Among many image processing techniques (2), particle tracking velocimetry (PTV) is one of the most effective techniques which enable us to make accurate velocity measurements in a variety of laboratory-scale flows of gases and liquids over a wide range of velocity (3).

The early attempt to apply PTV to three-dimensional flows was made by Chang and Tatterson (4) using stereoscopic photogrammetry with Bolex stereoscopic lens. Since this attempt, the principle of their 3D PTV was generally based on the similar stereoscopic image acquisition with the aid of multiple cameras (5), (6), (7), (8). While the minor differences are found in the recording techniques adopted by the 3D PTV techniques proposed in the past, it can be seen that they are essentially identical in terms of the stereoscopic recording of image sequences. However, the stereoscopic recording has fundamental problems since this method projects all of the tracer-particle images included in a measuring volume onto only a few two-dimensional frames. As a result, when the number of tracer particles largely increases, the procedures inherent in the previous 3D PTV, for example the identification of a particle image recorded by multiple cameras and the reconstruction of the three-dimensional particle positions, become almost impossible. This evidence is given by the fact that the numbers of the derived velocity vectors range from only around ten to several hundred at most in the previous measurements (9).

This study describes 3D PTV which makes use of a pair of optical scanners generating horizontally and vertically scanning laser-light sheets. The images of the tracer particles on the visualized sections are recorded by a high-speed video system capable of 500 frames per second, whose recording is synchronized with the scannings. Since the stereoscopic recording is discarded in the present 3D PTV, it is possible

to obtain quite larger number of velocity vectors than usual and the complicated calibration of multiple cameras is not necessary.

The digital image analyses are based on the numerical procedure proposed by Ushijima and Tanaka (1). In this method, several improvements have been made on the extraction of particle images, positioning of them with sub-pixel accuracy, determination of velocity vectors, variable tracking frame numbers and others. Consequently, the accuracy is made higher than the image analyses performed by the usual PTV. The derived velocity components are spatially interpolated with cubic spline functions at regular grid points in three-dimensional space and the theoretical model based on variational analysis is applied to the results so that the non-divergent conditions should be satisfied.

The developed 3D PTV is applied to the rotating fluids in a cubic cavity model equipped with a rotating disk. The secondary flows occurring on vertical sections as well as primary circulations caused by the rotating disk are quantitatively measured with the present 3D PTV. In addition, the flow patterns in the cavity are also numerically predicted and both results are compared.

PROCEDURE FOR IMAGE ACQUISITION

Flow visualization system

Figure 1 illustrates the manner of the flow visualization and the video recordings. A couple of scanners in this visualization system have small mirrors whose rotating shafts are arranged in different directions each other. As shown in Fig.1, the scanner-1 generates the vertical laser-light sheets which visualize multiple vertical sections. The visualized images are taken by a high-speed video cassette recorder (VCR) system through the front window of an experimental cavity model. On the other hand, the horizontal sections visualized by the scanner-2 are recorded with the same VCR system through a plane mirror placed below the transparent bottom window. Since the visualized horizontal and vertical sections are both included in the view of the high-speed video camera, only a single camera is needed in the present system.

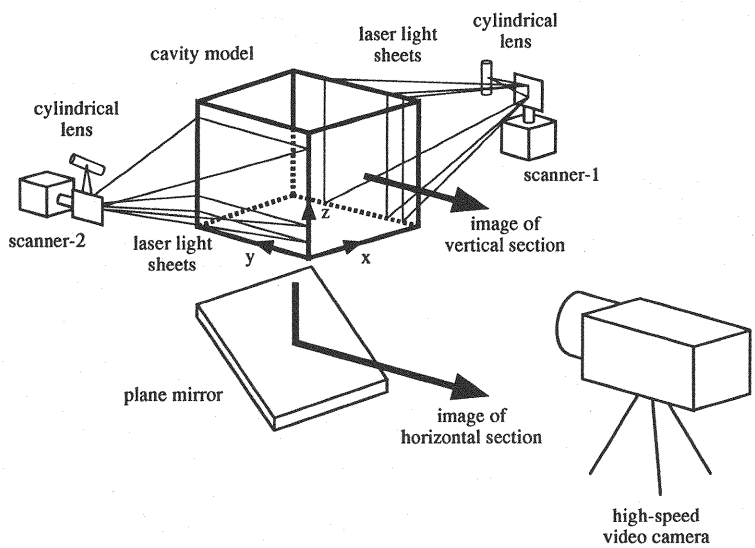

Fig.1 Flow visualization and image-recording system

The present VCR system (NAC HSV1000HS) is capable of taking 500 frames par second and its strobe (TTL) signals are utilized to synchronize the video recordings with the stepping movements of the scanners. Since two scanners are systematically operated by a control driver which receives the TTL signals from the VCR system, the continuously visualized sections are suitably recorded on the

appointed video frames. The exposure time per frame is set at 200 μs with the aid of an electrical shutter.

Cavity model with a rotating disk

It has been known that complicated three-dimensional flows are generally observed in rotating fluids as well as their primary circulating motions (10). In a cavity model equipped with a rotating disk on its upper boundary, secondary flows, as well as horizontal main circulations, are expected to appear on the vertical sections owing to the Ekman boundary layer developed near the bottom surface. Figure 2 shows a cubic cavity model with each side of 60 mm and a rotating disk 170 mm in diameter. The angular frequency ω of the rotating disk is set at $8\pi/15$ radian per second. The representative length scale L_0 is defined as the side length of the cavity (L_0 =60mm) and the Reynolds number based on L_0 and ω is estimated as about 6.0×10^3.

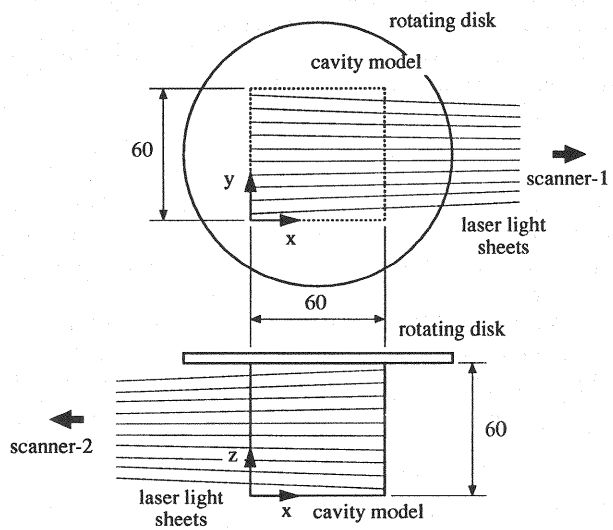

Fig.2 Cavity model with a rotating disk

Tracer particles scattered in the fluid are made of high polymer (Eslen) with a specific gravity of 1.03. Their average diameter is around 400 μm. Since these tracer particles include fluorescent sodium, their clear images can be taken in the presence of laser-light sheets. In experiments, the saline water with suitably-adjusted density is used as a working fluid so that the tracer particles can have completely neutral buoyancy.

As illustrated in Fig.2, the numbers of the visualized horizontal and vertical sections are 10 respectively and total 20 sections are recorded with the high-speed VCR system. Since two frames are recorded per section, the time interval between two adjacent sections is 4 ms and the scanning time cycle (T_C) corresponds to 80 ms. In the present measurements, 10 frames are recorded for each section during 10 scanning cycles which is equivalent to the sampling time (T_S) of 0.796 seconds.

DIGITAL IMAGE ANALYSES

Determination of particle positions

The images on a frame recorded by high-speed VCR system are transformed to digital data consisting of 512×512 pixels with 256-gray-level resolution per a single pixel. After applying adequate filters (11),

the particle images are separated from the background and their positions are determined with sub-pixel accuracy. This procedure is based on our previous numerical techniques (1).

The binarized images are first derived by means of the discriminant and least squares threshold selection as proposed by Otsu (12), which selects an optimum threshold level so that the summation of gray-level variances in two classes separated by the threshold should be minimum and that the variance between the two classes should be maximum on the basis of discriminant analysis. Instead of employing a single threshold level for a frame, the digital images on a frame are divided into 1,024 subregions each consisting of 16×16 pixels and the optimum threshold is determined for each subregion. The binarized particle image is then replaced by 3×3 pixels area without changing its center point. Finally, the logical products are taken between the original images having grey levels and the binarized particle images. This procedure allows us to separate the tracer particle images preserving 256-gray-level resolution from the background.

It is effective for the accurate positioning of the tracer particles to make use of their gray-level distributions, rather than the binarized results, since the error resulting from the incorrect positioning is a dominant factor for the total uncertainties of the derived velocity components. Thus the second-order regression curvature is derived for the gray-level distribution of each particle on the basis of the method of the least squares. Then the tracer particle position is determined with second-order accuracy as the point where the regression curvature gives its peak value.

Particle tracking

The particle tracking procedure as done by Ushijima and Tanaka (1) is applied to specify an identical particle recorded on the multiple frames. Figure 3 shows the search region on the $i+1$ frame, which is set up after the candidates of particle positions $(P_1, P_2, \ldots, P_i)$ have been specified. The center of the circular search region is set at $2\boldsymbol{p}_i - \boldsymbol{p}_{i-1}$, where $\boldsymbol{p}_i$ is the position vector of P_i. The radius of the search region r_i on the $i+1$ frame is set up as one-third of the average particle distance δ_{i+1} on the $i+1$ frame, which is one of the criteria to determine the search region employed by Malik et al. (13). When a single center point is located within the search region, this becomes a new candidate on the $i+1$ frame. In case that the multiple center points are included, the center point which gives the minimum variance of the local velocities calculated from P_{i-1}, P_i and P_{i+1} is selected. If there is no center point, all candidates $(P_1, P_2, \ldots, P_i)$ are discarded. This tracking procedure is repeated over N_T frames ($N_T \geq 3$), where N_T is referred to as tracking frame number.

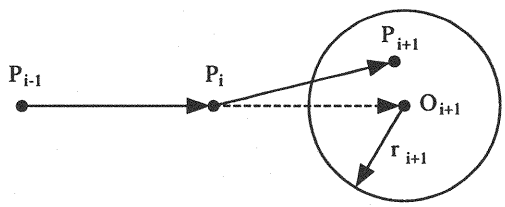

Fig.3 Search region on $i+1$ frame

On the first frame of tracking, the circular search region is set up, having its center at P_1 and its radius r_1 equals to $(1/2)\delta_1$. When multiple center points P_2 are included in the region, all of them are considered as valid and the tracking procedure described above continues to the following frames. While most of the mis-identified center points are dropped in the process of the multiple trackings, a group of center points which gives the minimum variance of local velocities derived from all center points is selected if more than two groups are finally obtained. If there is no second point P_2 in the search region, the corresponding first center point P_1 is discarded.

Since the tracking procedure for N_T frames is carried out throughout all of the sampled frames, changing the first frame of tracking one by one, the number of total tracking procedures is given by $N_S - N_T + 1$, where N_S is the sampled frame number. In the present method, the lower and upper limitations (N_{T1} and N_{T2} respectively) can be set for the tracking frame number in order to respond

to high and low velocity regions coexisting in the visualized area (1). Thus the tracking procedure is conducted L_T times, which is given by

$$L_T = (N_S + 1)(N_{T2} - N_{T1} + 1) - \sum_{k=N_{T1}}^{N_{T2}} k \tag{1}$$

Although the velocity components were usually derived only from the identified initial and terminal particle positions in previous works (14), (15), it is necessary for the accurate estimation of velocity vectors to take into consideration all intermediate particle positions as well as both ends. Thus, a quadratic function is approximated for a group of the identified positions with the method of least squares and the direction of velocity vector is defined as its tangential direction. In addition, the length of the velocity vector is calculated from the summation of all displacements (1).

When small number of error vectors are included in the results, bootstrap procedure (16) is utilized to remove them. The bootstrap technique enables us to derive a frequency distribution for each of the obtained velocity components. After evaluating the average μ and the standard deviation σ from the frequency distribution, the velocity component located outside of the bandwidth $\mu \pm 3\sigma$ are judged as errors and replaced by the average.

Three-dimensional velocity components

The velocity components obtained by the particle trackings are randomly distributed in accordance with the particle locations. Thus the results obtained by L_T times of tracking procedures are all superimposed and the average velocity vectors over the sampled frames are calculated at the appointed grid points. In terms of Nyquist sampling criterion, the resolution for the highest wavenumber is limited by $(1/2)\delta_V$ (17), where δ_V is the average distance of the velocity vectors, which implies that meaningful grid intervals should be larger than $2\delta_V$. Since δ_V is estimated as 1.05 mm in the present study, the regular grid points of 13×13×13 are set up in the cubic region in the cavity, which gives 5 mm interval between two adjacent grids. Two velocity components are first interpolated at the grid positions on the visualized sections. The weighted averaging based on the Gaussian window is utilized in the interpolation, whose window width is set at $1.24\delta_V$ as proposed by Agui and Jimenez (17). In this procedure, the error range for each interpolated result is also estimated with the bootstrap techniques as done by Ushijima and Tanaka (1), which will be utilized in the spatial smoothing as described later. As illustrated in Fig.2, the visualized sections are not parallel and another spatial interpolation is operated in the direction normal to the sections. For the velocity components interpolated on the horizontal sections, one-dimensional cubic spline functions are derived to interpolate them in the vertical direction. The similar procedure is conducted for the velocity components on the vertical sections. As a result, the error ranges as well as the three velocity components are obtained at the regular grid points. It is usual that the three-dimensional velocity components as obtained in laboratory measurements and in field observations do not completely satisfy the non-divergence condition even if they are carried out rigorously. The theoretical model based on variational analysis was proposed by Sasaki (18) and it was utilized by Sherman (19) to adjust the observed wind fields over complex terrain. This model is also adopted in the present study in order that the fluid continuity should be satisfied in each control volume. The specific function in this model is given by

$$E(u_i) = \int_v \left[\alpha_i^2 (u_i - u_{i0})^2 + \lambda \frac{\partial u_i}{\partial x_i}\right] dx_1 dx_2 dx_3 \tag{2}$$

where λ is the Lagrange multiplier. Here u_{i0} and u_i are measured velocity components and their adjusted values in x_i directions respectively, where x_i with $i = 1, 2$ and 3 correspond to x, y and z coordinates. While the values of α_i are Gauss precision moduli related to the measurement errors in u_i, these values are almost same regardless of their directions in the present case. Thus we may put $\alpha_1^2 = \alpha_2^2 = \alpha_3^2 \equiv \alpha^2$. The Euler-Lagrange equations to minimize $E(u_i)$ are given by

$$u_i = u_{i0} + \frac{1}{2\alpha^2} \frac{\partial \lambda}{\partial x_i} \tag{3}$$

$$\frac{\partial u_i}{\partial x_i} = 0 \tag{4}$$

and the equation for λ is derived as

$$\frac{\partial^2 \lambda}{\partial x_i^2} = -2\alpha^2 \frac{\partial u_{i0}}{\partial x_i} \tag{5}$$

The Eq.5 is discretized in a finite difference scheme and solved by a successive overrelaxation method. The boundary conditions are $\lambda = 0$ on the bottom surface and $\partial\lambda/\partial n = 0$ on the other boundaries. The obtained λ is substituted into Eq.3 and the adjusted velocity components are derived. Finally, as conducted by Agui and Jimenez (17), the velocity components are spatially smoothed by solving three-dimensional Laplace equations within the error ranges. As described above, the error ranges first obtained by the bootstrap method have already been interpolated at the grid points by means of cubic spline functions. The error ranges are now shifted so that the adjusted values for fluid continuity are taken into account:

$$err^i_{lmn} = \mu^i_{lmn} + \frac{1}{2\alpha^2}\frac{\partial \lambda}{\partial x_i} \pm \epsilon^i_{lmn} \tag{6}$$

Here $\mu^i_{lmn} \pm \epsilon^i_{lmn}$ are the error ranges for u_i obtained at the grid points P_{lmn}. The solutions of Laplace equations at $n+1$ step are compared with the shifted band widths calculated by Eq.6 and when they are not included in these ranges, they are replaced with the upper or lower limit values. Since the difference of the average discrete dilation before and after the smoothing procedure is less than 0.1% with respect to the representative quantity calculated from L_0 and ω, the non-divergence condition is effectively satisfied.

ROTATING FLUIDS MEASURED BY 3D PTV

Measurement conditions

In the measurements, the following conditions are adopted: the sampling frequency $f_S = 12.5$ (Hz), sampling time $T_S = 0.796$ (sec), tracking frame number $N_T = 4$ to 8, number of tracking procedure $L_T = 25$. The total number of the obtained vectors N_V equals 82,189. From N_V, the number of the vectors per visualized section (n_{VS}) and the number per a tracking procedure (n_{VT}) are calculated as 4,110 and 3,288 respectively. Taking account that the maximum number of the vectors captured by usual 3D PTV remains several hundred at most, it is demonstrated that quite larger number of vectors can be acquired with the present 3D PTV. The average of the absolute velocity components (V_0) is about 2.9 mm/s, which may be one of the representative quantities in the cavity flows. The sampling time T_S corresponds to 3.8% with respect to the time scale based on V_0 and L_0. Thus, it can be concluded that the effectively instantaneous velocity components are measured by the present 3D PTV.

Experimental Results

Figure 4 shows the distributions of velocity vectors on horizontal ($x-y$) and vertical ($x-z$) planes. The circulating flow patterns are observed in all horizontal sections and the intensity of velocity becomes weak near the bottom surface owing to the development of the Ekman boundary layer. While it can be seen that the circulating flows tend to diverge outside in the upper region in the cavity, the convergent circulations appear in the Ekman boundary layer in contrast. This typical flow pattern observed in a rotating fluid with Ekman boundary layers brings about the secondary flows observed on vertical sections; as shown in the $x-z$ section at y=30 mm, the ascending and descending flows arise in the center region and near the side boundaries respectively. As shown on the vertical sections at y=20 and 40 mm, the ascending flows are accompanied by circulation just outside of the center region.

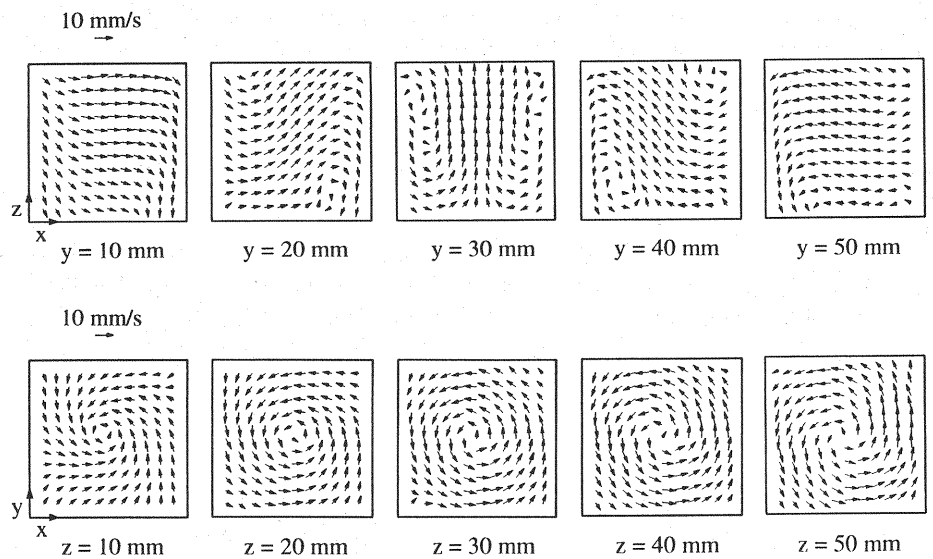

Fig.4 Measured velocity vectors with 3D PTV

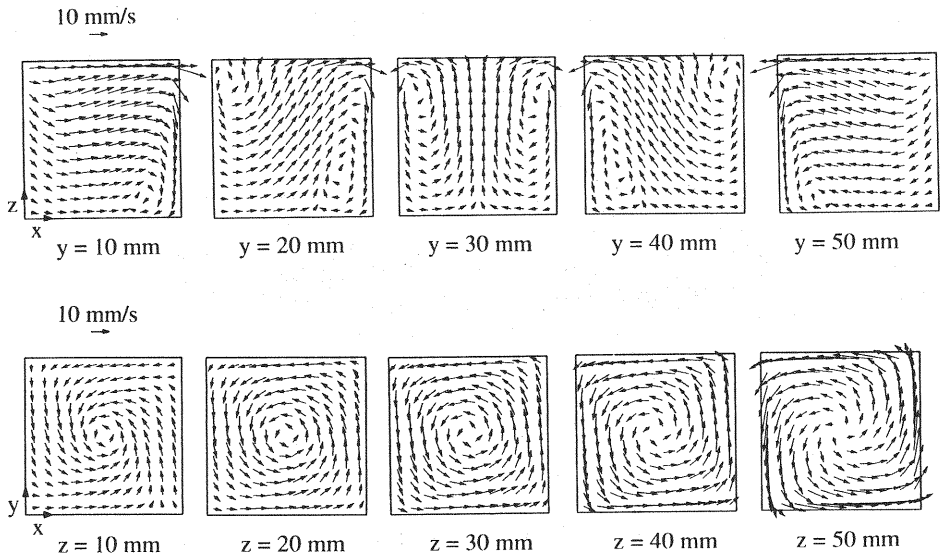

Fig.5 Calculated velocity vectors

Figure 5 shows the numerically predicted flows in the cavity. The numerical method follows the Lagrangian scheme discretization proposed by Ushijima (20). The cavity space is divided into 25×25×25 computational grids and steady flow patterns are obtained. Compared with the measured results in Fig. 4, while the discrepancies in the velocity intensity near boundaries may be found due to the different interval of the interpolating grids between experiments and computation, it can be seen that the overall flow patterns are agreed well each other. The measured three-dimensional flow patterns are visualized with the aid of computer graphics as shown in Fig.6. In this figure, the particles, initially located on a horizontal plane, are advected in the static velocity field which is assumed to be given by the measured results by the present 3D PTV. The time increment is 0.2 seconds and the particle positions are calculated by a Runge-Kutta method. As observed in Fig.6, the rotating ascending flow occurs in the center region of the cavity and the descending circulation appears near the side boundaries.

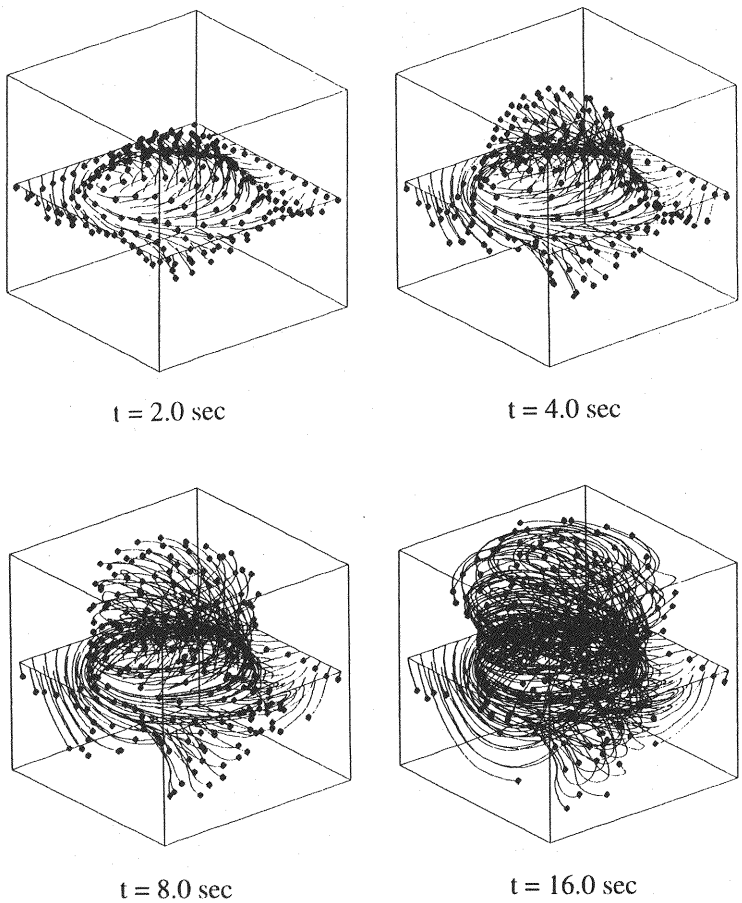

Fig.6 Visualized flow patterns

Estimation of Uncertainty

The uncertainties involved in PTV techniques have been widely investigated to specify the sources of errors and to evaluate their quantities (6), (14), (15), (17). The results of the previous works allow us to evaluate the uncertainties in the present 3D PTV. According to Agui and Jimenez (17), three

different errors, visualization error ϵ_{vis}, sampling error ϵ_{sam} and interpolation error ϵ_{int}, need to be taken into account. The visualization error consists of the positioning error of the particles (ϵ_η) and the error associated with the traceability of particles to the fluid motion (ϵ_f). The positioning error may be evaluated by

$$\epsilon_\eta = \eta^* V_0 \tag{7}$$

where η^* is the precision for a particle position normalized by the average length of the particle trajectories. Since the resolution of a pixel (Δ_p) corresponds to 120 μm and the average trajectory (Δ_t) is 0.93 mm, the present second-order positioning gives $\eta^* = (\Delta_p/\Delta_t)^2$ and the following result:

$$\epsilon_\eta = 1.67 \times 10^{-2} V_0 \tag{8}$$

On the other hand, the traceability error ϵ_f can be neglected in the present experiment, since the densities of the particles and the working fluid are almost same. The sampling error ϵ_{sam} is evaluated by the following equation:

$$\epsilon_{sam} = u' \left(\frac{3\eta_L V_0}{Du'} \right)^{(m-1)/(m+1)} \tag{9}$$

Here it is assumed that m=5/3 and $u'/V_0 = 0.1$ as done by Agui and Jimenez (17). Then we obtain

$$\epsilon_{sam} = 2.5 \times 10^{-2} V_0 \tag{10}$$

With reference to the results reported by Agui and Jimenez (17), the present interpolation error ϵ_{int} can be estimated of the same order as their values, since our interpolation method is substantially based on their procedures: a convolution with an adaptive Gaussian window with the same window width (1.24δ), Class-3 bootstrap estimation and others. Assuming that the interpolation error is 3%, the total error ϵ_T is calculated from the summation of the squares as

$$\epsilon_T = 4.2 \times 10^{-2} V_0 \tag{11}$$

It is concluded that the present 3D PTV possibly involves about 4.2% uncertainty with respect to the representative velocity.

CONCLUDING REMARKS

A 3D PTV system, which enables us to obtain quite larger number of velocity vectors than usual, has been developed in order to measure effectively instantaneous all velocity components in the three-dimensional space. The developed system utilizes a pair of optical scanners which can generate horizontally and vertically scanning laser-light sheets. The images of the tracer particles on the visualized sections are recorded by a high-speed VCR system capable of 500 frames per second, whose recording is synchronized with the scannings. Since the usual stereoscopic recording by multiple cameras is dismissed, the present 3D PTV becomes free from the major drawbacks involved in previous 3D PTV: for example, identification of a particle image recorded by multiple cameras, camera calibrations and reconstruction of the three-dimensional particle positions. As a result, the number of the acquired velocity vectors becomes roughly ten times as many as that of the usual techniques (9), which results in the higher spatial resolution in the present system.

The developed 3D PTV was applied to the rotating fluids in a cubic cavity model equipped with a rotating disk. This 3D PTV enables us to capture the primary circulating flows and vertical secondary flow patterns, which are typically observed in a rotating fluid with Ekman boundary layers. The agreement of measured and numerically predicted flow patterns are satisfactory. In the measurements, more than 82,000 vectors are acquired within the sampling time of 0.796 seconds, which allows us to derive nearly 3,300 vectors per a single tracking procedure. Taking account that the maximum number of the vectors captured by usual 3D PTV remains several hundred at most, it can be concluded that the present 3D PTV is quite advantageous in terms of spatial resolution.

REFERENCES

1. Ushijima, S. and Tanaka, N. : Particle tracking velocimetry using laser-beam scanning and its application to transient flows driven by a rotating disk, ASME Journal of Fluids Engineering, Vol.116, pp.265-272, 1994.

2. Hesselink, L. : Digital image processing in flow visualization, Annual Review of Fluid Mechanics, 20, pp.421-485, 1988.

3. Adrian, R. J. : Particle-Imaging Techniques for Experimental Fluid Mechanics, Annual Review of Fluid Mechanics, 23, pp.261-304, 1991.

4. Chang, T.P. and Tatterson, G.B. : An automated analysis method for complex three dimensional mean flow fields, Proceedings 3rd International Symposium on Flow Visualization, pp.266-273, 1983.

5. Adamczyk, A. A. and Rimai, L. : Reconstruction of a 3-dimensional flow field from orthogonal views of seed track video images, Experiments in Fluids, 6, pp.380-386, 1988.

6. Nishino, K., Kasagi, N. and Hirata, M. : Three-dimensional particle tracking velocimetry based on automated digital image processing, ASME Journal of Fluids Engineering, Vol.111, pp.384-391, 1989.

7. Sata, Y. and Kasagi, N. : Improvement toward high measurement resolution in three-dimensional particle tracking velocimetry, Proceedings 6th International Symposium on Flow Visualization, Springer-Verlag, 1992.

8. Maas, H. G., Gruen, A. and Papantoniou, D. : Particle tracking velocimetry in three-dimensional flows, Experiments in Fluids, 15, pp.133-146, 1993.

9. Kasagi, N and Nishino, K. : Probing turbulence with three-dimensional particle-tracking velocimetry, Experimental Thermal and Fluid Science, 4(5), pp.601-612, 1991.

10. Greenspan, H. P. : The theory of rotating fluids, Cambridge Univ. Press, 1968.

11. Rosenfeld, A. and Kak, A.C. : Digital picture processing, Academic Press, Inc., 1976.

12. Otsu, N. : Discriminant and least squares threshold selection, Proceedings 4th International Joint Conference on Pattern Recognition, pp.592-596, 1978.

13. Malik, N. A., Dracos, Th and Papantoniou, D. A. : Particle tracking velocimetry in three-dimensional flows part II: particle tracking, Experiments in Fluids, 15, pp.279-294, 1993.

14. Imaichi, K. and Ohmi, K. : Numerical processing of flow-visualization pictures – measurement of two-dimensional vortex flow, Journal of Fluid Mechanics, Vol. 129, pp.283-311, 1983.

15. Kobayashi, T., Yoshitake, Y., Saga, T. and Segawa, S. : An image processing technique for determining two-dimensional flow fields with reverse flow, Proceedings ASME Symposium on Physical and Numerical Flow Visualization, pp.39-46, 1985.

16. Efron, B., : Estimating the error rate of a prediction rule: improvement of cross-validation, Journal of American Statistical Association, Theory and Methods Section, Vol.78, No.382, 316-331, 1983.

17. Agui, J. and Jimenez, J. : On the performance of particle tracking, Journal of Fluid Mechanics, Vol.185, pp.447-468, 1987.

18. Sasaki, Y. : Numerical variational analysis formulated under the constraints determined by longwave equations and lowpass filter, Monthly Weather Review, 98, pp.884-898, 1970.

19. Sherman, C. A. : A mass-consistent model for wind fields over complex terrain , Journal of Applied Meteorology, 17, pp.312-319, 1978.

20. Ushijima, S. : Prediction of thermal stratification in a curved duct with 3D boundary-fitted coordinates, International Journal for Numerical Methods in Fluids, Vol.19, pp.647-665, 1994.

APPENDIX-NOTATION

The following symbols are used in this paper:

L_0 = side length of a cavity model;
L_T = number of tracking procedures;
N_S = sampled frame number;
N_T = tracking frame number;
N_{T1} = lower limitation of N_T;
N_{T2} = upper limitation of N_T;
N_V = number of the obtained velocity vectors;
n_{VS} = N_V per a visualized section;
n_{VT} = N_V per a tracking procedure;
P_i = particle position on i-th frame;
r_i = radius of a searching region for P_i;
T_C = scanning time cycle;
T_S = sampling time;
u_{i0} = measured velocity component;
u_i = adjusted velocity component;
V_0 = average of absolute velocity components;
α_i = Gaussian precision moduli;
δ_i = average particle distance on i-th frame;
δ_V = average distance of velocity vectors;
ϵ_η = positioning error;
ϵ_f = traceability of particles to fluid motion;
ϵ_{sam} = sampling error;
ϵ_T = total error;
λ = Lagrangian multiplier;
μ = average of bootstrap samples;
σ = standard deviation of bootstrap samples;
ω = angular frequency of a rotating disk;

(Received March 4, 1997; revised April 17, 1998)